Tuning metal-insulator behavior in LaTiO₃/SrTiO₃ heterostructures integrated directly on Si(100) through control of atomic layer thickness

Kamyar Ahmadi-Majlan¹, Tong-Jie Chen², Zheng Hui Lim¹, Patrick Conlin¹, Ricky Hensley¹, Matthew Chrysler¹, Dong Su³, Hanghui Chen⁴, Divine P. Kumah², and Joseph H. Ngai^{1*}

We present electrical and structural characterization of epitaxial LaTiO₃/SrTiO₃ heterostructures integrated directly on Si(100). By reducing the thicknesses of the heterostructures, an enhancement in carrier-carrier scattering is observed in the Fermi liquid behavior, followed by a metal to insulator transition in the electrical transport. The insulating behavior is described by activated transport, and its onset occurs near 1 electron per Ti occupation within the SrTiO₃ well, providing evidence for a Mott driven transition. We also discuss the role that structure and gradients in strain could play in enhancing the carrier density. The manipulation of Mott metal-insulator behavior in oxides grown directly on Si opens the pathway to harnessing strongly correlated phenomena in device technologies.

*jngai@uta.edu, §dpkumah@ncsu.edu

¹Department of Physics, University of Texas-Arlington, Arlington, TX 76019, USA

²Department of Physics, North Carolina State University, Raleigh, NC 27695, USA

³Center for Functional Nanomaterials, Brookhaven National Laboratory, Upton, NY11973, USA

⁴Institute of Physics, New York University Shanghai, Pudong, Shanghai 200122, China

Elucidating how the behavior of electronic materials evolves as material dimensions approach the nanoscale is of great fundamental and technological importance as device technologies continue to shrink to smaller length scales. Transition metal oxides that exhibit strongly correlated phenomena are of particular interest, given their high carrier densities, short electronic length scales, and diverse range of phases they possess. Recent advancements in thin film epitaxy have enabled correlated oxide films to be grown with thicknesses that approach fundamental electronic length scales (*e.g.*, Thomas-Fermi screening length). At such length scales, altering the thickness by merely one or two unit-cells can have a profound effect on the stability of electronic phases. Interfaces between oxides have also emerged as a setting in which high density electron gases or liquids can be created and rich correlated phenomena observed. In essence, interfaces in layered oxide heterostructures enable artificial correlated materials to be realized.

In this regard, artificial heterostructures exhibiting Mott driven metal-insulator (MI) transitions are of fundamental and technological interest. Rare-earth titanates are an archetype example of a so-called filling-controlled Mott system, in which the MI transition is driven by carrier density. In bulk rare-earth titanates, carrier density is tuned through chemical composition. In comparison, carrier density in layered heterostructures can be tuned through confinement or electric field-effect. Such artificial Mott systems could introduce additional functionalities in nanoscale devices used for information processing or sensing. Thus, achieving Mott-driven MI behavior in oxide heterostructures integrated directly on technologically relevant platforms is important.

Here we present the electrical and structural characterization of rare-earth oxide heterostructures integrated directly on Si(100). 15,16 Our heterostructures are comprised of the Mott insulator LaTiO₃ (LTO) and band insulator SrTiO₃ (STO). 12 At (100)-oriented heterojunctions between LTO and STO, an electron liquid is created in the latter, due to a transfer of charge from the former. $^{14,17-19}$ For our heterostructures, oxygen vacancies in STO further enhance the sheet carrier densities n_s measured. Evidence for Mott-like MI behavior in the transport characteristics of the heterostructures is observed. Nominally thick wells are metallic, exhibiting transport characteristics described by Fermi liquid behavior. By reducing the thickness of the heterostructures, carrier-carrier scattering is enhanced, and a MI transition is induced. Activated transport over a large temperature regime is observed in the insulating phase,

and the onset of insulating transport occurs as the carrier density within the heterostructure approaches 1 electron per Ti. The control of Mott MI transitions in oxides grown directly on Si opens the pathway to harnessing such strongly correlated phenomena in device technologies.

Our heterostructures are comprised of n unit-cells (u.c.) of STO on Si, followed by 3 u.c. of LTO and 1.5 u.c. of STO on top, as illustrated in the inset of Fig. 1(b). A detailed schematic of our heterostructures (Fig. S1) and methods for growth and characterization can be found in the Supplementary Information. Prior studies of rare-earth titanate/STO heterostructures grown on single crystal oxide substrates found that 3 u.c. of the rare-earth titanate was necessary to maximize charge transfer. ^{7,14} The heterostructures exhibit atomically abrupt interfaces between STO and Si and STO and LTO, as shown in the high angle annular dark-field (HAADF) image of the n = 6 heterostructure in Fig. 1(a). The Hall signal was found to be linear up 5 T, the maximum field applied during measurement. We find that n_s 's for all the heterostructures are ~ 2 to 2.6×10^{15} cm⁻², at 250 K, which is much higher than the $\sim 3.5 \times 10^{14}$ cm⁻² expected strictly from charge transfer from LTO to STO. 6,20,21 We attribute the higher n_s to oxygen vacancies in STO created during deposition of LTO under the relatively low O₂ pressures necessary to avoid the formation of an insulating La₂Ti₂O₇ phase, ¹⁵ and also from a brief anneal of the STO in vacuum to improve crystallinity. The n_s 's remain largely invariant with temperature (Fig. S2(d)), though a slight decrease is observed in some of the heterostructures. Carrier mobilities (Fig. S2(e)) are similar to those measured on rare-earth titanate/STO heterostructures grown on single crystal oxide substrates that have comparable STO thickness. 14 Carriers transferred from the LTO to the top 1.5 u.c. of STO are likely localized given the thinness of the STO. However, we found that the thin STO cap was necessary to maximize n_s in the STO layers below, as was the use of an additional capping layer of amorphous silicon deposited in situ at room temperature after growth (Fig. S2(f) and (g)). Both minimize effects of surface depletion and over oxidation of the LTO in ambient air. 7,22 Thus, our heterostructures can be thought of as having itinerant carriers within a STO channel situated between LTO and Si.

A MI transition is observed in the transport characteristics of our heterostructures as the thickness of the STO n decreases, as shown in Fig.1(b). Insulating samples are defined as those in which $dR_s/dT < 0$ throughout the temperature range of measurement. For reference, the 2D quantum of resistance (grey dashed line, Fig. 1(b)) is shown. The MI transition exhibits characteristics consistent with a transition that is driven by strong correlations, as opposed to

disorder. First, Fermi liquid behavior is observed on the metallic side of the transition, which is characterized by a quadratic temperature dependence of R_s given by $R_s = AT^2 + R_0$, as shown in Fig. 1(c). As the transition is approached with decreasing n, the A parameter of the Fermi liquid T^2 dependence increases, as summarized in Fig. 1(d). The increase in A corresponds to an increase in the effective mass of the carriers, which is a signature of enhanced electron-electron scattering in bulk rare-earth titanates. $^{1.6,12,13,23}$ Second, the insulating behavior in our heterostructures is described by Arrhenius, *i.e.* activated, transport as shown in the fit (red-dashed) in Fig. 1(e). In contrast, disorder driven insulating behavior is typically described by variable-range-hopping. We note that the temperature range over which Arrhenius behavior is observed is virtually identical to the range found in bulk LTO. 12 Third, the activation energies E_A 's extracted from fitting the insulating transport data of the n = 5 and 6 heterostructures to the Arrhenius function are exceptionally small (~ 2 and 3 meV, respectively), consistent with a system that is very close in proximity to a MI transition. Fourth, the slight increase in E_A observed between the n = 6 and n = 5 heterostructures (inset of Fig. 1(e)) denotes a continued trend in enhanced correlations.

We now turn to the structural characterization of our LTO/STO heterostructures. Synchrotron X-ray diffraction reveals a rapid relaxation in epitaxial strain in the heterostructures. The basic perovskite lattice constants of bulk LTO, STO and that of the (100) surface of Si are 3.95 Å, 3.91 Å and 3.84 Å, respectively. Figure 2(a) shows reciprocal space maps (RSM) for n = 5, 6, 7, 11 samples around the off-axis reflection of Si (2, 2, L) for which there is no overlap with a Si Bragg peak. The RSMs are plotted in terms of the reciprocal lattice unit (r. l. u.) of bulk Si $(2\pi \cdot 5.431^{-1} \text{ Å}^{-1})$. Note the diffracted intensity centered at H = K = 2, L = 2.702 Si r.l.u. labelled C on the n = 5 RSM in Fig. 2(a), denoting the presence of a component of the heterostructure that is coherently strained to the Si substrate. Less intense spectral weight is observed at lower H = K and larger L values on the n = 5 RSM (labelled A and B), indicating the presence of partially relaxed components of the heterostructure and gradients in strain. As n increases by just a single unit-cell, the relative intensity of the coherently strained (partially relaxed) component(s) C (A, B) decreases (increases), as shown more clearly in the line profile plots of Fig. 2(b). The extracted in-plane and out-of-plane lattice constants of components A, B and C are compared in Table S1 for the n = 5, 6, 7 and 11 heterostructures. Based on the lattice constants extracted, we

attribute components A and B to partially relaxed STO/LTO and STO respectively, while component C corresponds to the fraction of the STO that is coherently strained to the Si.

Film relaxation occurs via the formation of dislocations, which provides an extrinsic source of carrier scattering. However, carrier scattering from dislocations cannot explain the MI transition that we observe. Analysis of the linewidths of the RSMs reveals that for the thinner (thicker), insulating (metallic) heterostructures, carriers traverse a region of STO that has a longer (shorter) coherence length (Table S2). To experimentally rule out extrinsic origins to the MI behavior, we have also studied ultrathin films of $La_{0.75}Sr_{0.25}TiO_3$ films grown on Si. We find that $La_{0.75}Sr_{0.25}TiO_3$ films ($n_s \sim 4 \times 10^{15}$ cm⁻²) of comparable thickness to the insulating heterostructures remain metallic, indicating that the emergence of insulating behavior is a characteristic of the heterostructure, and not a generic effect of reducing the thickness of nominally metallic oxide films grown on Si (see Fig. S3). Though conduction through the LTO layer cannot be ruled out, the LTO layer alone cannot account for the MI behavior, since all heterostructures have 3 u.c. of LTO. Finally, parallel transport from spatially separated carriers in STO and LTO channels also cannot account for the key characteristics of the MI transition, particularly the enhancement in A with decreasing n, which we discuss below.

To account for the enhancement of A with decreasing n in the Fermi liquid behavior, followed by insulating activated transport, we analyze the MI behavior within the context of strong correlations, which is a hallmark feature of rare-earth titanates. One possible explanation of the MI behavior is a filling-controlled Mott transition, driven by a 3-dimensional carrier density n_{3D} of 1 electron per Ti site ($\sim 1.6 \times 10^{22}$ cm⁻³), achieved by reducing the thickness of the STO channel. In this regard, we note that similar studies of layered rare-earth titanate/STO heterostructures grown on single crystal oxide substrates also found evidence for Mott-like MI behavior driven by increasing n_{3D} .

To explore how a Mott transition could arise, we present a heuristic model that estimates n_{3D} using coupled Poisson and Schrödinger equations.²⁵ The insulating n=6 heterostructure for which the onset of insulating behavior occurs is modelled as a ~ 24 Å wide STO well situated between Si and LTO, in which the z-coordinate z=0 (z=-24 Å) represents the STO/LTO (Si/STO) interface. The carrier density n_{3D} is obtained from $n_{3D}(z)=\frac{m^*}{\pi\hbar^2}\sum_i(E_F-E_i)|\psi_i(z)|^2$ in which the sub-band energies E_i and $\psi_i(z)$ are found by numerically diagonalizing the Schrödinger equation. We use m^* of ~ $4m_e$ (m_e = bare electron mass) which is appropriate for

the Ti t_{2g} bands of STO.^{26,27} E_F is determined by filling occupied sub-bands i until $n_s \sim 2 \times 10^{15}$ cm⁻² is reached, which is the value of n_s for the n=6 heterostructure. The carrier potential V is determined by iteratively solving the Poisson $\nabla^2 V = -\rho_f(z)/\epsilon(E)$ and Schrödinger equations. $\rho_f(z)$ is comprised of $n_{3D}(z)$, positive ionized La ion cores situated at z=0, as well oxygen vacancies in the STO, which we model using an exponentially decaying profile $\rho_{ox} \propto e^{z/\kappa}$ for which z < 0, and $\kappa = 8$ Å. The latter assumes oxygen migrates towards the surface during the brief anneal in vacuum immediately prior to LTO deposition. A 0.2 V drop in potential at the interface between STO and Si is used to model the type-II band arrangement between the former and latter. ²⁸ Finally, our model also accounts for the electric-field dependent dielectric constant of STO via $\epsilon(E(z)) = 1 + \epsilon_0^{-1} \partial P/\partial E$, where P is related to E(z) through the Landau-Ginzburg-Devonshire free energy. ²³ Figure 3(a) shows the calculated n_{3D} , revealing that $n_{3D} \sim 1.6 \times 10^{22}$ cm⁻³ is indeed possible given the n_s and confinement of our heterostructures.

In regards to the transport behavior near the MI transition, linear behavior in the magnetoresistance is observed (Fig. S4), consistent with percolative transport. Percolative transport could arise from phase separation, which is commonly observed in metal oxides exhibiting MI transitions. The dependence of n_{3D} on z from the LTO/STO interface (Fig. 3(a)) could also introduce spatial variation in the electronic properties. Thus, the transport characteristics we measure reflect an average behavior over all such forms of nanoscale variation.

Finally, we make a few remarks on the effect that physical structure could have on n_{3D} . The gradient in strain in the STO channel could enhance n_{3D} through an electric field E_{STO} produced by the flexoelectric effect. To understand the origin of E_{STO} , we note that the strained components of STO for the n = 5, 6, and 7 heterostructures exhibit anomalously large c/a ratios that indicate that the volume of the STO unit-cell is not conserved. Prior studies revealed that this non-conservation in unit-cell volume arises from non-centrosymmetric displacements of the Ti cations, which gives rise to a large upward polarization, as illustrated in the inset of Fig. 3(b). 30,31,32 As the heterostructure becomes thinner, the polarization of the strained component of STO (component C) increases, as evidenced by the c/a ratios shown in Fig. 3(b) for the n = 5, 6, 7 and 11 heterostructures. The horizontal dashed line in Fig. 3(b) indicates the c/a ratio above (below) which strained STO is polar (non-polar). We note that *ab initio* density functional theory (DFT) calculations also predict the upwards polarization in STO even with the presence of LTO

on top, as summarized in Fig. S5. The coherently strained component of STO, however, is only \sim 2 - 3 u.c. thick, as the compressive strain decays very rapidly towards the LTO. Figure 3(c) illustrates the relaxation of the coherently strained component of STO for the n = 5 heterostructure. Analysis of the RSM indicates that within \sim 2 u.c. the extracted in-plane lattice a increases from 3.84 Å to 3.89 Å, *i.e.* essentially bulk STO (see Table S1). Such a gradient in strain can, in principle, generate an electric field via the flexoelectric effect that would enhance n_{3D} by compressing the carriers towards the LTO.^{33,34} We estimate E_{STO} could be as large as \sim 8 \times 10⁷ V/m using an approach that is independent of the mechanism for film relaxation (see Supplemental Information).³⁴

In summary, we have demonstrated atomic-scale control of strong correlations and MI behavior in LTO/STO heterostructures integrated directly on Si(100). Evidence for Mott driven MI behavior is observed, namely, an enhancement in electron-electron scattering as the MI transition is approached and insulating behavior described by activated transport. Supporting this picture, calculations indicate that and a carrier density in STO of 1 electron per Ti is possible in our heterostructures. Oxide heterostructures on silicon in which strong correlations can be tuned through thickness could be exploited as channel materials in emerging field-effect devices, or be exploited in sensors or even in energy harvesting, as recently proposed. 35,36,37 The material behavior of strongly correlated oxides complements the properties of conventional semiconductors, and would lead to additional modalities in device functionality.

SUPPLEMENTARY MATERIAL

Additional electrical and structural characterization as well as density-functional theory calculations can be found in the Supplementary Material.

ACKNOWLEDGMENTS

This work was supported by the National Science Foundation (NSF) under award No. DMR-1508530 and the University of Texas-Arlington under the Research Enhancement Program. We also thank the Alan G. MacDiarmid Nano Tech Institute at the University of Texas-Dallas for use of the Quantum Design PPMS. STEM work is supported by the Center for Functional

Nanomaterials, Brookhaven National Laboratory, which is supported by the U.S. Department of Energy (DOE), Office of Basic Energy Science, under Contract No. DE- SC0012704. We express our gratitude to S. Ismail-Beigi for providing the code for the Poisson-Schrödinger solver.

REFERENCES

- ¹M. Imada, A. Fujimori and Y. Tokura, Rev. Mod. Phys. **70**, 1039 (1998).
- ²D. P. Kumah, A. S. Disa, J. H. Ngai, H. -H. Chen, A. Malashevich, J. W. Reiner, S. Ismail-Beigi, F. J. Walker and C. H. Ahn, Adv. Mater. **26**, 1935 (2014).
- ³P. D. C. King, H. I. Wei, Y. F. Nie, M. Uchida, C. Adamo, S. Zhu, X. He, I. Bozovic, D. G. Schlom and K. M. Shen, Nat. Nanotech. **9**, 443 (2014).
- ⁴A. Ohtomo and H. Y. Hwang, Nature **427**, 423 (2004).
- ⁵J. Mannhart and D. G. Schlom, Science **327**, 1607 (2010).
- ⁶P. Moetakef, C. A. Jackson, J. Hwang, L. Balents, S. J. Allen and S. Stemmer, Phys. Rev. B **86**, 201102(R) (2012).
- ⁷P. Xu, Y. Ayino, C. Cheng, V. S. Pribiag, R. P. Comes, P. V. Sushko, S. A. Chambers and B. Jalan, Phys. Rev. Lett. **117**, 106803 (2016).
- ⁸A. D. Caviglia, S. Gariglio, N. Reyren, D. Jaccard, T. Schneider, M. Gabay, S. Thiel, G. Hammerl, J. Mannhart and J. M. Triscone, Nature **456**, 624 (2008).
- ⁹J. Biscaras, N. Bergeal, A. Kushwaha, T. Wolf, A. Rastogi, R. C. Budhani and J. Lesueur, Nat. Comm. **1**, 89 (2010).
- ¹⁰L. Li, C. Richter, J. Mannhart and R. C. Ashoori, Nat. Phys. 7, 762 (2011).
- ¹¹J. H. Ngai, F. J. Walker and C. H. Ahn, Annu. Rev. Mater. Res. 44, 1 (2014).
- ¹²C. C. Hays, J. -S. Zhou, J. T. Markert and J. B. Goodenough, Phys. Rev. B **60**, 10367 (1999).
- ¹³Y. Tokura, Y. Taguchi, Y. Okada, Y. Fujishima, T. Arima, K. Kumagai and Y. Iye, Phys. Rev. Lett. **70**, 2126 (1993).
- ¹⁴P. Moetakef, T. A. Cain, D. G. Ouellette, J. Y. Zhang, D. O. Klenov, A. Janotti, C. G. Van de Walle, S. Rajan, S. J. Allen and S. Stemmer, Appl. Phys. Lett. **99**, 232116 (2011).

- ¹⁵E. N. Jin, L. Kornblum, . D. P. Kumah, K. Zou, C. C. Broadbridge, J. H. Ngai, C. H. Ahn and F. J. Walker, APL Mater. **2**, 116109 (2014).
- ¹⁶L. Kornblum, E. N. Jin, D. P. Kumah, A. T. Ernst, C. C. Broadbridge, C. H. Ahn and F. J. Walker, Appl. Phys. Lett. **106**, 201602 (2015).
- ¹⁷A. Ohtomo, D. A. Muller, J. L. Grazul and H. Y. Hwang, Nature **419**, 378 (2002).
- ¹⁸S. Okamoto and A. J. Millis, Nature **428**, 630 (2004).
- ¹⁹J. S. Kim, S. S. A. Seo, M. F. Chisholm, R. K. Kremer, H. -U. Habermeier, B. Keimer and H. N. Lee, Phys. Rev. B **82**, 201407(R) (2010).
- ²⁰M. Takizawa, H. Wadati, K. Tanaka, M. Hashimoto, T. Yoshida, A. Fujimori, A. Chikamatsu, H. Kumigashira, M. Oshima, K. Shibuya, T. Mihara, T. Ohnishi, M. Lippmaa, M. Kawasaki, H. Koinuma, S. Okamoto and A. J. Millis, Phys. Rev. Lett. 97, 057601 (2006).
- ²¹S. S. A. Seo, W. S. Choi, H. N. Lee, L. Yu, K. W. Kim, C. Bernhard and T. W. Noh, Phys. Rev. Lett. **99**, 266801 (2007).
- ²²A. Ohtomo and H. Y. Hwang, Appl. Phys. Lett. **84**, 1716 (2004).
- ²³P. Nozieres and D. Pines, *The Theory of Quantum Liquids* (Westview Press, Boulder,1999).
- ²⁴L. Bjaalie, A. Janotti, B. Himmetoglu and C. G. Van de Walle, Phys. Rev. B **90**, 195117 (2014).
- ²⁵J. H. Ngai, Y. Segal, D. Su, F. J. Walker, S. Ismail-Beigi, K. Le Hur and C. H. Ahn, Phys. Rev. B **81**, 241307(R) (2010).
- ²⁶O. Copie, V. Garcia, C. Bodefeld, C. Carretero, M. Bibes, G. Herranz, E. Jacquet, J.-L. Maurice, B. Vinter, S. Fusil, K. Bouzehouane, H. Jaffres and A. Barthelemy, Phys. Rev. Lett. **102**, 216804 (2009).
- ²⁷L. F. Mattheiss, Phys. Rev. B **6**, 4718 (1972).
- ²⁸F. Amy, A. Wan, A. Kahn, F. J. Walker and R. A. McKee, J. Appl. Phys. **96**, 1601 (2004).

- ²⁹W. -N. Lin, J. -F. Ding, S. -X. Wu, Y. -F. Li, J. Lourembam, S. Shannigrahi, S. -J. Wang and T. Wu, Adv. Mater. Inter. **1**, 1300001 (2014).
- ³⁰D. P. Kumah, J. W. Reiner, Y. Segal, A. M. Kolpak, Z. Zhang, D. Su, Y. Zhu, M. S. Sawicki, C. C. Broadbridge, C. H. Ahn and F. J. Walker, Appl. Phys. Lett. **97**, 251902 (2010).
- ³¹J. C. Woicik, H. Li, P. Zschack, E. Karapetrova, P. Ryan, C. R. Ashman and C. S. Hellberg, Phys. Rev. B **73**, 024112 (2006).
- ³²A. M. Kolpak, F. J. Walker, J. W. Reiner, Y. Segal, D. Su, M. S. Sawicki, C. C. Broadbridge, Z. Zhang, Y. Zhu, C. H. Ahn and S. Ismail-Beigi, Phys. Rev. Lett. **105**, 217601 (2010).
- ³³P. Zubko, G. Catalan and A. K. Tagantsev, Annu. Rev. Mater. Res. 43, 387 (2013).
- ³⁴D. Lee, A. Yoon, S. Y. Jang, J.-G. Yoon, J.-S. Chung, M. Kim, J. F. Scott and T. W. Noh, Phys. Rev. Lett. **107**, 057602 (2011).
- ³⁵X. Hong, J. Phys. Condens. Matter **28**, 103003 (2016).
- ³⁶M. Eckstein and P. Werner, Phys. Rev. Lett. **113**, 076405 (2014).
- ³⁷E. Manousakis, Phys. Rev. B **82**, 125109 (2010).

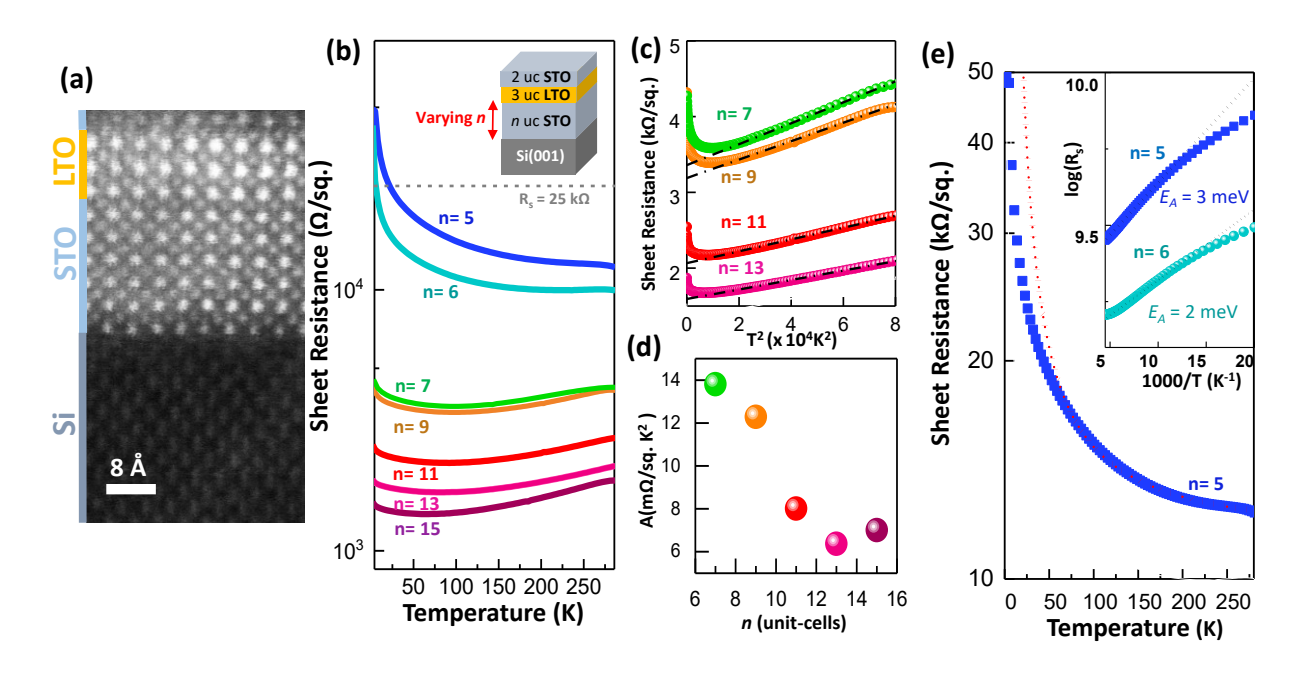


FIG. 1. (a) STEM HAADF image of the n=6 heterostructure. (b) Sheet resistance of STO/LTO/STO/Si heterostructures of different thicknesses showing metal-insulator transition. The 2D Mott minimum conductivity is indicated by the dashed line. (c) Sheet resistance for metallic STO/LTO/STO/Si heterostructures plotted versus T^2 . The dashed-dot lines are fits to the Fermi-liquid equation. (d) Temperature coefficient A as a function of thickness for metallic samples. (e) Sheet resistance for insulating n=5 heterostructure. The red dotted line is a fit to Arrhenius law. The inset shows sheet resistance plotted against 1/T for the insulating n=5 and 6 heterostructures. Black dotted lines are fits to the activated transport, with activation energies shown.

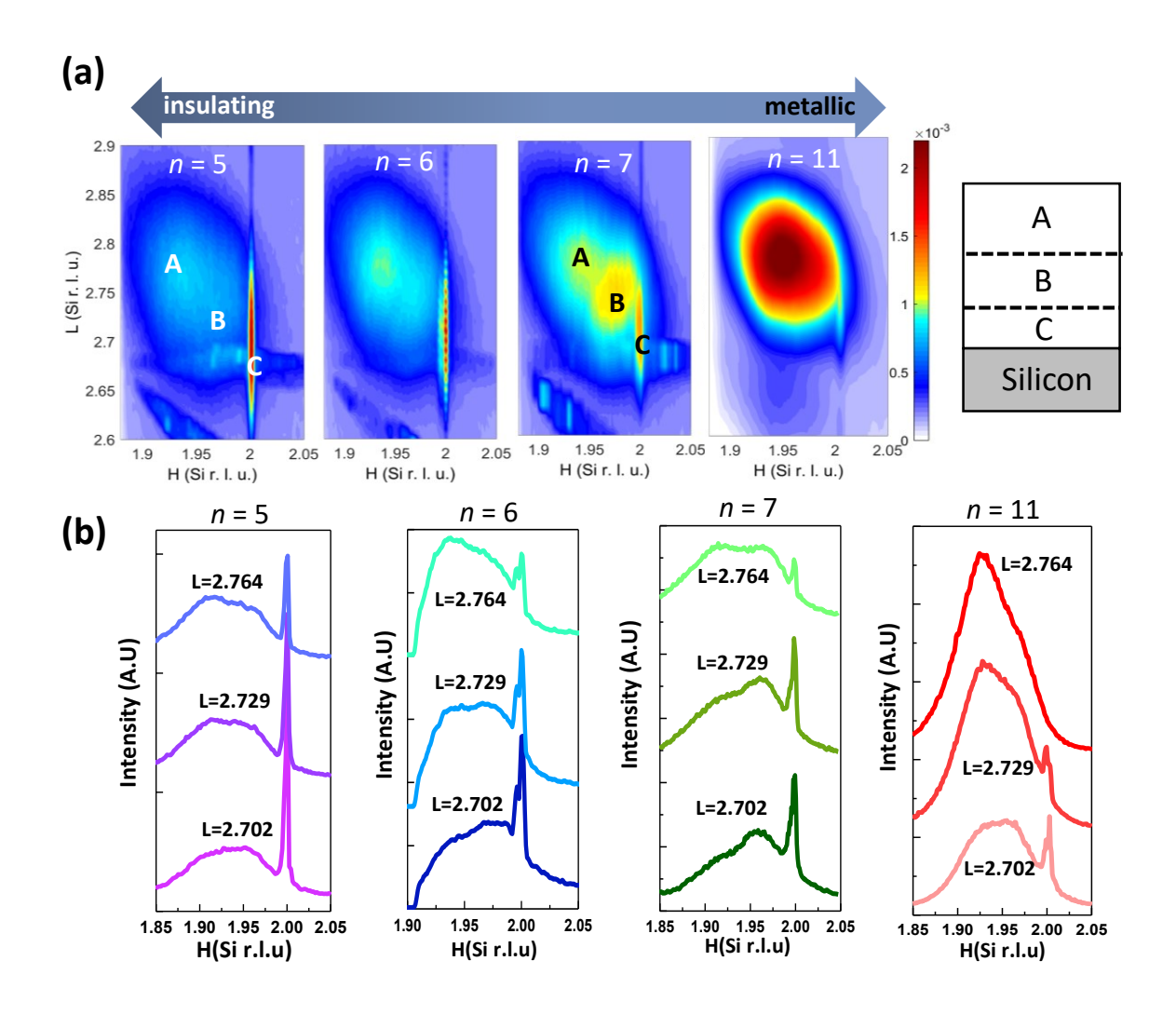


FIG. 2. (a) Reciprocal space maps taken of heterostructures of various thickness n, showing the partially relaxed (labelled A, B) and coherently strained regions (labelled C). (b) Line profile plots of the RSMs shown in (a).

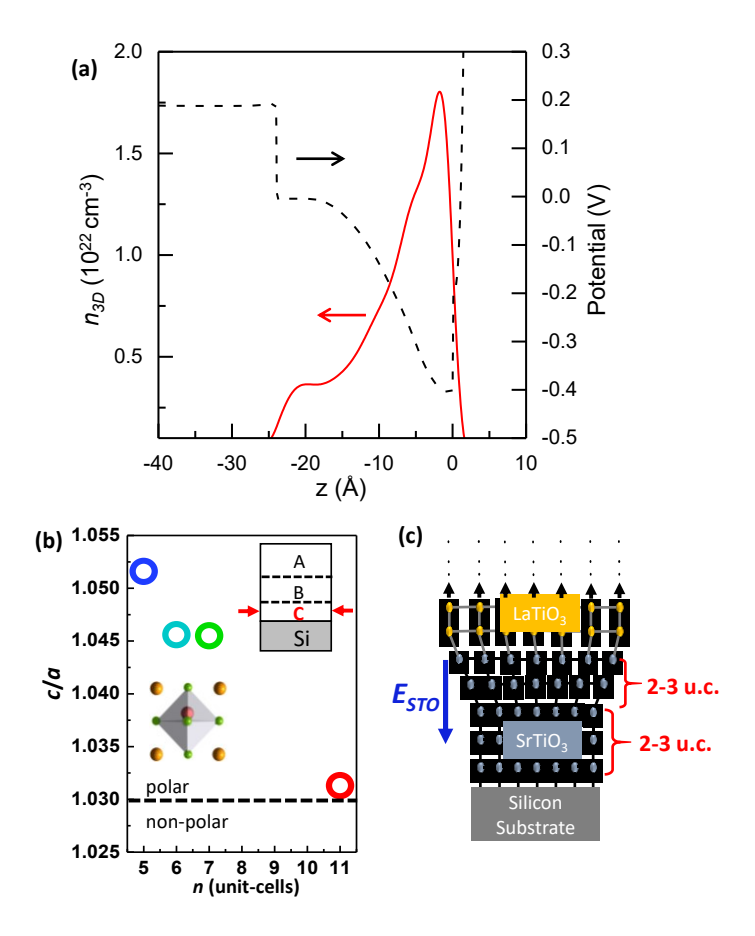


FIG. 3. (a) n_{3D} calculated from a Poisson-Schrödinger model showing carrier density equivalent to 1 electron per Ti. (b) Ratio between c to a lattice constants for the component of STO ('C') that is coherently strained to Si (top inset). The anomalously large c/a ratios indicate the STO exhibits a polarization, illustrated in the bottom inset. (c) Schematic illustrating the thickness of the coherently strained STO and the number of unit-cells over which strain relaxes for the n = 5 heterostructure. The gradient in strain can produce an electric field via the flexoelectric effect.